JCTC Journal of Chemical Theory and Computation

Understanding the Resonance Raman Scattering of Donor−Acceptor Complexes using Long-Range Corrected DFT

Daniel W. Silverstein and Lasse Jensen*

Department of Chemistry, The Pennsylvania State University, 104 Chemistry Building, University Park, Pennsylvania 16802

Abstract: The optical properties involving charge-transfer states of the donor−acceptor electron-transfer complexes carbazole/tetracyanoethylene (carbazole/TCNE) and hexamethylbenzene/tetracyanoethylene (HMB/TCNE) were investigated by utilizing the time-dependent theory of Heller to simulate absorbance and resonance Raman spectra. Excited-state properties were obtained using time-dependent density functional theory (TDDFT) using the global hybrid B3LYP and the long-range corrected LC-ωPBE functionals and compared with experimental results. It is shown that, while reasonable simulations of the absorbance spectra can be made using B3LYP, the resonance Raman spectra for both complexes are poorly described. The LC-ωPBE functional gives a more accurate representation of the excited-state potential energy surfaces in the Franck−Condon region for charge-transfer states, as indicated by the good agreement with the experimental resonance Raman spectrum. For the carbazole/TCNE complex, which includes contributions from two overlapping excited states on its absorbance spectrum, interference effects are discussed, and it is found that detuning from resonance with an excited state results in interference along with other factors. Total vibrational reorganization energy for both complexes is discussed, and it is found that both B3LYP and LC-ωPBE yield reasonable estimates of this quantity compared with experiment.

Introduction

Electron-transfer reactions are fundamental processes involved in chemistry and biology. Some important applications of these processes include studies of photocatalysis,[1,2] charge transfer (CT) in polymers,[3] and numerous other biological and chemical processes.[4−6] Resulting from those applications, investigations involving the rate of electron transfer and optimization of that process are a major research focus.

For molecules that undergo a change in oxidation state due to electron transfer, the molecular geometry changes as well. The rate of electron transfer between molecules strongly depends on molecular geometries of the donor and acceptor molecules before and after the electron-transfer event.[7−9] A more quantitative analysis of structural changes due to

electron-transfer requires knowledge of which normal modes are Franck−Condon (FC) active, because it is these modes that are strongly influenced by electron transfer. Using resonance Raman spectroscopy allows the CT state being investigated to be characterized and the information about the rate of electron transfer to be quantified.[7,8,10−12]

Several methods for modeling resonance Raman scattering have been developed. In the vibronic theory of Albrecht et al.,[13−15] the Born−Oppenheimer (BO) approximation is used to separate each vibronic state into a product of the electronic and vibrational wave functions. Then, the transition dipole moment is expanded as a Taylor series in the nuclear coordinates. This allows the Raman transition polarizability to be represented as a sum of terms, where the first is the A term (FC) and the second is the B term (Herzberg−Teller). Another formulation is the time-dependent formalism developed by Heller et al.[16−21] This method uses wave packet dynamics to describe the time-dependent overlap of the final

* Corresponding author. E-mail: jensen@chem.psu.edu.

state and the initial vibrational wave function that propagates along the excited-state potential energy surface. Unlike the vibronic theory, the time-dependent method avoids the computationally demanding summation over intermediate vibrational states.[16,19,22] Both methods can be used with harmonic approximations of the ground- and excited-state potential energy surfaces that are displaced along the normal coordinate, in the independent mode displaced harmonic oscillator (IMDHO) method.[21] Excited-state displacements calculated using the IMDHO method are proportional to the excited-state gradient at the ground-state equilibrium geometry, which can be used to model resonance Raman spectra and also be applied to studying electron-transfer rates using Marcus theory.[7,8,10]

Density functional theory (DFT) has been applied in several cases for studying vibronic structure of molecules in resonance Raman scattering.[23–25] Traditional DFT exchange−correlation (XC) functionals have been shown to largely underestimate the CT excitations of weakly interacting systems,[26–29] but this effect has been demonstrated to be partially corrected using the long-range corrected (LC) DFT.[30–33] Although many studies have shown the usefulness of LC-DFT for correctly describing CT excitation energies,[30–33] there has not been a study of resonance Raman scattering of CT excited states using the LC functionals. This will provide an additional validation of the LC functionals since it is crucial to accurately describe the curvature of the excited-state surface for correctly modeling resonance Raman scattering.

Here we will present a detailed study of the resonance Raman scattering of two donor−acceptor complexes using LC-DFT combined with Heller's time-dependent theory of Raman scattering. Time-dependent density functional theory (TDDFT) is used to evaluate excited-state displacements within the IMDHO method for the hexamethylbenzene/tetracyanoethylene (HMB/TCNE) and carbazole/tetracyanoethylene (carbazole/TCNE) complexes. The absorption and resonance Raman scattering spectra are then simulated using the time-dependent theory. Complexes similar to those studied in this work have been investigated using the LC-functional BNL (Baer−Neuhauser−Livshits)[33,34] to investigate how the attenuation parameter in that functional can be tuned to give improved descriptions of excitation energies for CT states in comparison to experiment.[35] For both of these systems, their resonance Raman scattering have been measured experimentally,[36–38] thus enabling a comprehensive comparison between theory and experiment. The low-energy portion of the optical absorbance spectra for these complexes include excitations where an electron is transferred from the donor (carbazole or HMB) to the acceptor (TCNE) molecule.[36–38] The complex HMB/TCNE has a single CT state on its absorbance spectrum, while carbazole/TCNE has two energetically close CT states that overlap in one band on the absorbance spectrum. For the carbazole/TCNE complex, contributions from two CT states result in interference effects, which have been observed in previous studies that focused on experimentally derived fits to resonance Raman spectra.[37,39,40] Total vibrational reorganization ener-

gies are also compared between the XC functionals and experiment for both complexes.

Theory

Expressions for the absorbance cross-section (σ_a) and Raman polarizability ($\alpha_{\rho\lambda}^n$) can be obtained by applying both the FC and BO approximations. In the time-dependent formalism, expressions for σ_a and $\alpha_{\rho\lambda}^n$ can be rewritten as respective full- and half-Fourier transforms, resulting in[16–21]

$$\sigma_a = \frac{4\pi}{3\hbar c} E_L \sum_n (\mu^{0n})^2 \times \mathrm{Re} \int_0^\infty \langle i|i_n(t)\rangle e^{i(E_L+\nu_{i0})t - \Gamma_n t - (1/2)\Theta^2 t^2} dt \tag{1}$$

and

$$\alpha_{\rho\lambda}^n = \sum_n \mu_\rho^{0n} \mu_\lambda^{n0} \times i \int_0^\infty \langle f|i_n(t)\rangle e^{i(E_L+\nu_{i0})t - \Gamma_n t - (1/2)\Theta^2 t^2} dt \tag{2}$$

For both expressions, E_L defines the energy of the incident radiation, n defines the electronic state (where 0 is the electronic ground state), μ^{0n} defines the electronic transition dipole moment for an excitation between electronic states 0 and n, ν_{i0} is the energy of vibrational state $|i\rangle$, and $|i_n(t)\rangle = e^{-i\hat{H}_n t/\hbar}|i\rangle$ is the wavepacket corresponding to the time-dependent nuclear wave function of electronic state n. The homogeneous broadening for this system is treated phenomenologically with the addition of Γ_n, which allows for each excited state to have a different lifetime. It is often difficult to fit absorbance spectra with only the homogeneous broadening parameter Γ_n because the Lorentzian line shape resulting from $\exp(-\Gamma t)$ decays too slowly, which is found to worsen the fit on the red edge of the absorption spectrum.[20] This can be compensated by including an inhomogeneous broadening parameter, Θ, where both eqs 1 and 2 represent convolutions of Gaussian and Lorentzian line shapes (Voigt line shape). In particular for the Raman polarizability[41,42] given in eq 2, the final vibrational state $|f\rangle$ is involved in the dynamics, and the subscripts ρ and λ refer to x, y, and z directions of the transition dipole moment vectors and polarizability tensor elements.

In order to calculate the overlaps between different vibrational states, the IMDHO model[16,20,21] was used. This method relies on assumptions that the ground- and excited-state potential energy surfaces are harmonic and have the same normal-mode composition and frequencies. The excited-state displacement relative to the ground-state equilibrium position of the potential is given by the shift Δ_k^n in dimensionless normal coordinates. Use of the IMDHO method allows for the overlap integrals to be written

$$\langle i|i_n(t)\rangle = e^{-\sum_j s_j^n(1-e^{-i\omega_j t}) - i(\nu_{i0}-E_{0n})t} \tag{3}$$

for determining the absorption cross-section and

$$\langle f|i_n(t)\rangle = \prod_k \left\{ \frac{(-1)^{m_k}(\Delta_k^n)^{m_k}}{(2^{m_k} m_k!)^{1/2}} (1 - e^{-i\omega_k t})^{m_k} \right\} \times$$
$$e^{-\sum_j s_j^n(1-e^{-i\omega_j t}) - i(\nu_{i0}-E_{0n})t} \tag{4}$$

Donor–Acceptor Complexes

J. Chem. Theory Comput., Vol. 6, No. 9, 2010 **2847**

for the Raman polarizability. For these expressions, $s_k^n = (\Delta_k^n)^2/2$ are the Huang–Rhys factors, and m_k is the excitation number for the kth normal mode of vibrational state $|f\rangle$.

After determining the Raman polarizabilities, the differential Raman scattering cross-section can be calculated to compare with experimental measurements.[43–45] For measurements of scattered radiation 90° from the direction of propagation of the incident radiation, the differential Raman scattering cross-section is given by

$$\frac{d\sigma}{d\Omega} = \frac{\pi^2}{\varepsilon_0^2}(\nu_{in} - \nu_{k0})^4 \left(\frac{45a_k^2 + 7\gamma_k^2}{45}\right) \times$$

$$\frac{1}{1 - \exp[-hc\nu_{k0}/k_B T]} \quad (5)$$

where ν_{in} is the energy of the incident radiation and T is the temperature (assumed to be 300 K in the present work). The tensor invariants a_k and γ_k are the isotropic and anisotropic polarizability averages, given by

$$a_k = \frac{1}{3}\{(\alpha_{xx})_k + (\alpha_{yy})_k + (\alpha_{zz})_k\} \quad (6)$$

and

$$\gamma_k^2 = \frac{1}{2}\{[(\alpha_{xx})_k - (\alpha_{yy})_k]^2 + [(\alpha_{yy})_k - (\alpha_{zz})_k]^2 +$$

$$[(\alpha_{zz})_k - (\alpha_{zz})_k]^2 + 6[(\alpha_{xy})_k - (\alpha_{yz})_k + (\alpha_{zx})_k]^2\} \quad (7)$$

In order to perform the integrals for obtaining the absorbance cross-section and Raman polarizability, the dimensionless excited-state displacements (Δ_k^n) must be calculated. When the potential energy surface is assumed to be harmonic,[21] Δ_k^n relates to the partial derivative of the excited-state electronic energy with respect to a ground-state normal mode at the ground-state equilibrium position:

$$\left(\frac{\partial E^n}{\partial q_k}\right)_{q_k=0} = -\nu_{k0}\Delta_k^n \quad (8)$$

The excited-state electronic energy gradients in eq 8 are calculated using a three-point central differences formula around the ground-state equilibrium geometry. For convenience, the derivatives are initially determined in mass-weighted normal coordinates, Q_k, not the dimensionless normal coordinates q_k. However, it is easy to convert between the two using the relationship:[46]

$$\frac{\partial E^n}{\partial q_k} = \left(\frac{dQ_k}{dq_k}\right)\frac{\partial E^n}{\partial Q_k} = \sqrt{\frac{\hbar}{2\pi c\nu_{k0}}}\frac{\partial E^n}{\partial Q_k} \quad (9)$$

Excited-state electronic energy gradients in terms of mass-weighted normal coordinates were evaluated using formulas similar to those presented by Reiher et al. for numerical derivatives of the polarizability tensor elements,[47] replacing the polarizability with electronic energy at positions displaced along each normal mode.

Electron-transfer rates for harmonic potential energy surfaces can be quantified if the energy penalty for transferring an electron, i.e. the energy difference between the charge-separated state at the equilibrium geometry of both the neutral system and the charge-separated state, is known. This energy penalty is called the reorganization energy, λ_{tot}.[9] Generally, λ_{tot} is partitioned into two components, the solvent reorganization energy (λ_s) and vibrational reorganization energy (λ_ν), as

$$\lambda_{tot} = \lambda_s + \lambda_\nu \quad (10)$$

The solvent reorganization energy is the energy cost resulting from solvent molecules reorienting themselves after the electron transfer takes place, in order to optimize the solvent–complex interactions. Vibrational reorganization energy results from changes in the molecular geometry due to electron transfer. For a harmonic free energy surface, the total vibrational reorganization energy can be written as a sum of single-mode contributions

$$\lambda_\nu = \frac{1}{2}\sum_k (\Delta_k^n)^2 \nu_{k0} = \sum_k \lambda_{\nu,k} \quad (11)$$

Analysis of the single-mode contributions to the vibrational reorganization energy compared with what is found experimentally yields complementary information to examining the features of resonance Raman spectra.

Computational Details

In the long-range corrected (LC) approach, the interelectronic repulsion is partitioned into separate short- and long-range terms, which is given for electronic separation r_{12} as

$$\frac{1}{r_{12}} = \frac{1 - \text{erf}(\omega r_{12})}{r_{12}} + \frac{\text{erf}(\omega r_{12})}{r_{12}} \quad (12)$$

where ω is the attenuation parameter, the first term on the right side of eq 12 is for the short-range part of the exchange, and the second term of the right side of that equation is used for the long-range part of the exchange. Recently, we implemented several LC functionals into NWChem[48] based on the general approach produced by Hirao and co-workers[30] for constructing the short-range generalized gradient approximation (GGA) XC functional.[49,50] An alternative procedure based on a model for the Perdew–Burke–Ernzerhof (PBE) exchange hole has been presented by Scuseria and co-workers.[51,52] LC functionals based on this procedure, LC-ωPBE and LC-ωPBEh, have been shown to lead to a good description of both ground- and excited-state properties.[53] Here we have implemented these functionals into NWChem.[48]

The ground-state equilibrium geometry and normal modes for the HMB/TCNE and carbazole/TCNE complexes were determined using the B3LYP functional[54] and 6-31G* basis set. Normal-mode frequencies were scaled by 0.98 from the B3LYP values to obtain better agreement with experimental frequencies. Optical properties, including excited-state energies used for determining the dimensionless displacements, were calculated using the TDDFT linear response method[55,56] in NWChem. The dimensionless displacements were calculated based on the B3LYP structure, and the normal modes using either B3LYP or LC-ωPBE were used for calculating the excitation energies. For the LC-ωPBE functional, ω was
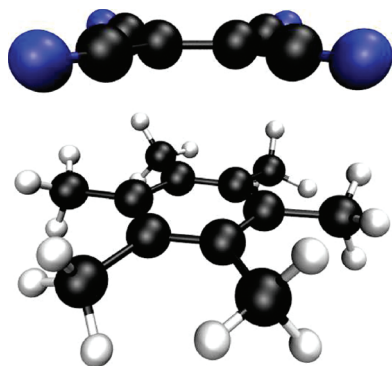
Figure 1. Optimized structure for the HMB/TCNE complex using B3LYP/6-31G*.

chosen to be $0.30a_0^{-1}$. This value is based on previous applications where it was shown that this value leads to the best performance for excited-state properties, such as excitation energies.[53,57] Excitation energies using the LC-ωPBEh functional yielded very similar results to the LC-ωPBE functional and are thus not reported.

Simulation parameters for the absorbance spectrum were determined by shifting the peak position and changing the peak width to match the experimental absorbance spectrum using a mixture of homogeneous and inhomogeneous broadening. Peak height was normalized to match the experimental absorbance spectrum by applying a scale factor to the DFT results. Repositioned excitation energies and homogeneous and inhomogeneous broadening parameters for each functional were then used to simulate the resonance Raman spectra. The scale factors used to normalize the absorbance maxima were not applied to the resonance Raman spectra. Additional details of the fitting procedure are described in the Supporting Information.

Results and Discussion

HMB/TCNE. The structure for the HMB/TCNE complex is shown in Figure 1. In this system, the electron-donor molecule is HMB, and the electron acceptor is TCNE. Experimentally, the absorbance maximum is found to be located at 532 nm (2.33 eV) with a transition dipole moment estimated at 1.644 au.[37] The LC-ωPBE functional places the excitation at 499 nm (2.48 eV) with a transition dipole moment of 1.218 au, while B3LYP finds the excitation to

be at 668 nm (1.86 eV) with a transition dipole moment of 1.597 au. LC-ωPBE locates the excited state closer to where it is found experimentally than B3LYP. Discrepancies between the experimental and the theoretical excitation energies may be attributed to solvent effects that are not included in the TDDFT calculations and the basis set dependence of the excitation energies.

Simulated absorbance spectra for the HMB/TCNE complex obtained using B3LYP and LC-ωPBE are shown in Figure 2. Also, shown in Figure 2 is the simulated absorbance spectrum using data fitted to the experimental spectrum taken from ref 37. For this complex, one symmetric peak is observed with an absorbance maximum positioned at 532 nm that corresponds to an intermolecular charge-transfer state between the HMB donor and TCNE acceptor. Calculations using LC-ωPBE find that the first excitation is the highest occupied molecular orbital (HOMO)-1 to lowest unoccupied molecular orbital (LUMO) transition, which is a dark state, while the second excitation is the HOMO to LUMO transition that is a bright state. In this case, both the HOMO and HOMO-1 come from HMB, and the LUMO is from TCNE. B3LYP yields a similar character for the frontier molecular orbitals, however, it reorders the energy and the intensity of the two excitations.

Examination of Figure 2 shows that each method gives a reasonably accurate model of the experimental data. It is coincidental that each method uses the same homogeneous broadening parameter Γ, but the inhomogeneous broadening is dominant due to its much larger magnitude. The variation in the Δ_k^n values is reflected in part by the inhomogeneous broadening parameter Θ which varies from 1000 cm^{-1} for the experimental fitted data to 1800 cm^{-1} for the B3LYP functional. Also, it is apparent that each description differs because each fit is scaled by a different factor. While the Δ_k^n values from B3LYP and experiment cause the absorbance cross-section to be overestimated by about 25%, using Δ_k^n values from LC-ωPBE results in the underestimation of the absorbance cross-section by about the same factor. The scale factor that is applied to the experimental fit, in this case, is likely due to the different model for the inhomogeneous broadening used in this work compared to the original work of Myers et al.[37]

Resonance Raman spectra simulated at 530 nm with the optimum modeling parameters for the absorbance spectra are

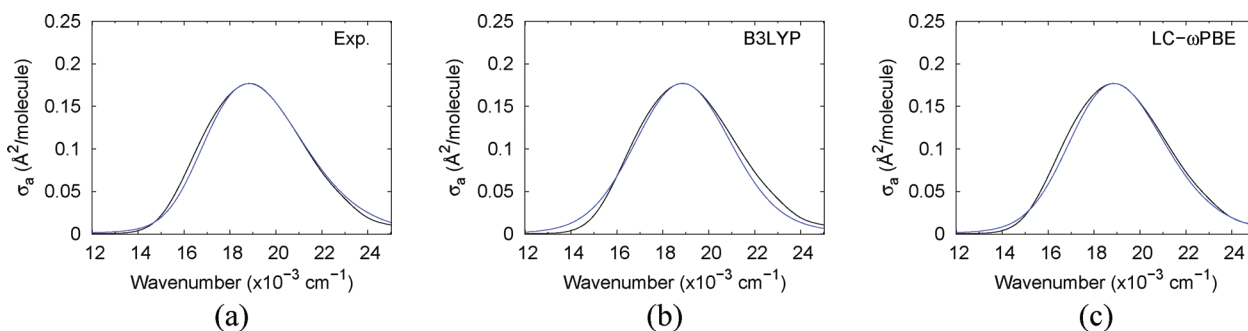| | | |
| (a) | (b) | (c) |

Figure 2. Absorbance spectra for HMB/TCNE with fits (blue line) compared to the experimental absorbance spectrum (black line, ref 37). The fit to experimental data (labeled "Exp.") used $\Gamma = 300$ cm^{-1}, $\Theta = 1000$ cm^{-1}, and scale factor = 0.725. Using the B3LYP functional: $\Gamma = 300$ cm^{-1}, $\Theta = 1800$ cm^{-1}, and scale factor = 0.761. For LC-ωPBE: $\Gamma = 300$ cm^{-1}, $\Theta = 1400$ cm^{-1}, and scale factor = 1.29.
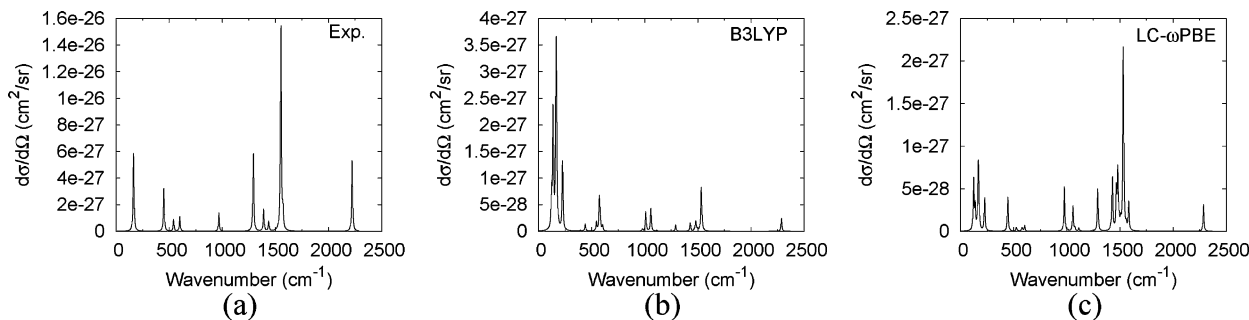
Figure 3. Resonance Raman spectra at 530 nm for HMB/TCNE using the optimum modeling parameters for the absorbance spectra plotted in Figure 2. Data for the spectrum labeled "Exp." are from ref 37. Spectra are broadened with a Lorentzian function with 10 cm^{-1} width.

presented in Figure 3 using B3LYP and LC-ωPBE. For comparison we also plot the simulated Resonance Raman spectrum using the data obtained by fitting to the experimental spectrum, which we will refer to as the experimental spectrum since it is essentially identical to what was found by Myers et al.[37] A qualitative comparison of the B3LYP spectrum with the experimental resonance Raman spectrum indicates that B3LYP significantly underestimates the relative peak intensities of the high-energy normal modes. Comparing the data from the LC-ωPBE functional with the experimental resonance Raman spectrum shows that LC-ωPBE yields much better agreement with experiment. For both experiment and LC-ωPBE, the most intense peak results from the C=C stretch at 1570 cm^{-1} on the TCNE structure, whereas for B3LYP it involves the intermolecular donor−acceptor (D−A) stretching motion at 165 cm^{-1} (see Supporting Information for complete normal mode assignments).

There are some noticeable differences between the spectrum from LC-ωPBE and the experimental spectrum. The region around 1000 cm^{-1} has only one important mode (due primarily to a C−CH$_3$ stretch and CH$_3$ deformation on HMB) in the experimental spectrum, but LC-ωPBE indicates there are two modes with similar mode structure and intensity at 956.85 and 1056.58 cm^{-1}. Also, LC-ωPBE overestimates the intensities of several modes between 1460 and 1500 cm^{-1} relative to the large peak at 1531.11 cm^{-1}. It is also found that the lower frequency region (below 250 cm^{-1}) has some additional features, but these low-frequency modes are not very accurately described in the harmonic approximation. Inclusion of anharmonic effects in the model would be a method to test if anharmonicity is important, but this is not feasible for large molecular systems like the HMB/TCNE complex. There may also be an improvement in the description of these modes if solvent effects are included in the TDDFT calculations, which have been shown to be important for describing intramolecular CT states of rhodamine 6G.[25] It may also be important to include dispersion corrections to the XC functional in complexes, such as HMB/TCNE, like those used in the DFT-D method.[58,59]

Quantitative inspection of the peak intensities of the different resonance Raman spectra show that the agreement between theory and experiment is not perfect, but it is interesting that changing between the two XC functionals yields such a dramatic change in relative peak intensities. The resonance Raman spectrum simulated with LC-ωPBE

yields differential Raman scattering cross-sections that differ by a range of factors between 4 and 10 when compared with those derived experimentally. A similar comparison between the spectrum from B3LYP and that from experiment shows that, resulting from the poor description of the high-energy normal modes, the differential Raman scattering cross-sections vary by a range of a factor of 2 to a large factor of approximately 50 for some of the higher energy normal modes. Based on the good agreement between spectra plotted with LC-ωPBE and experiment, it appears that the long-range corrections to the XC potential are necessary for describing the electronic structure in systems where CT states are important.

Further evidence of the necessity of long-range corrections to the XC potential for the HMB/TCNE system are shown on the low-energy side of the resonance Raman spectra. For the normal mode at 165 cm^{-1}, it is found that the motion of the system involves vibrations where the HMB and TCNE molecule change relative distance from one another. In situations where molecules involved in a CT excitation change distance from one another, it has been shown that the excitation energy[26,53] and the potential energy surface[60] are dependent on the distance R between the donor and acceptor molecule. As the intermolecular distance is changed for a CT state, it is expected that the interactions between the cationic donor molecule (HMB) and anionic acceptor molecule (TCNE) behave as $1/R$, so the potential energy surface should have that behavior. Resonance Raman spectra, and especially the excited-state gradients used for determining Δ_k^n values, are a useful probe of how well the excited-state potential energy surface is described by the XC functional.

For B3LYP, although the magnitude of the Δ_k^n for the intermolecular D−A stretch is comparable to that determined experimentally (2.80 from B3LYP compared with −3.80 from experiment), this is likely a result of fortuitous error cancellation because the rest of the Δ_k^n values are poorly described using this functional. The experimental result for the sign of Δ_k^n for this mode was rationalized based on the fitting procedure by including the nuclear coordinate dependence on the transition dipole moment (Herzberg−Teller terms).[37] Note that for a single contributing excited state, the sign of Δ_k^n is irrelevant as long as Duschinsky rotations are not accounted for,[61] and also that experimentally measured resonance Raman spectra can only yield the
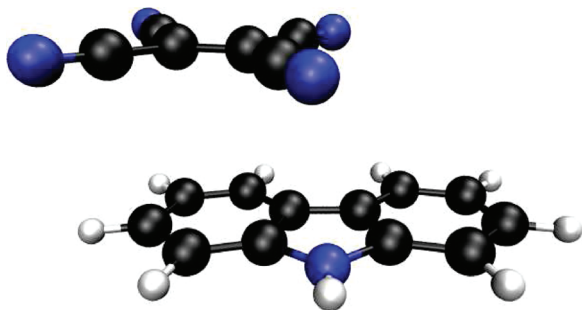
Figure 4. Optimized structure carbazole/TCNE complex using B3LYP/6-31G*.

Table 1. TDDFT Results for the Vertical Excitation Energies and Magnitudes of the Transition Dipole Moments Compared with the Experimental Estimates of These Values[37]

	CT1			CT2		
method	λ (nm)	energy (eV)	$\|\|\mu^{on}\|\|$ (au)	λ (nm)	energy (eV)	$\|\|\mu^{on}\|\|$ (au)
B3LYP	1138	1.09	0.579	836	1.48	1.496
LC-ωPBE	549	2.26	0.740	487	2.55	0.785
experiment[36]	626	1.98	1.531	536	2.31	0.822

absolute value of Δ_k^n. The potential energy surface described by B3LYP displays a shape that is incorrect, likely attributed to the incorrect exponential decay of XC potential. LC-ωPBE has a slightly worse agreement for this mode with experiment (Δ_k^n is 2.12 for LC-ωPBE compared with -3.80 from experiment), but the rest of the spectrum is described much more similarly to the experimental results. This finding reflects the importance of asymptotic decay of the XC potential in this system.

It is also interesting to compare the methods based on the vibrational reorganization energy. The total reorganization energies for experiment,[37] B3LYP, and LC-ωPBE are 3517, 2140, and 2738 cm^{-1}, respectively. Comparing these values indicates both DFT methods underestimate the reorganization energies, by approximately 1400 and 800 cm^{-1} for B3LYP and LC-ωPBE, respectively. This partially reflects that both B3LYP and LC-ωPBE underestimate the value of Δ_k^n for almost every mode when compared with the fit determined experimentally. Another cause for the difference between

the Δ_k^n values is that those calculated from TDDFT are for the HMB/TCNE complex in vacuum, but those determined experimentally include the effects of solvent. Inclusion of solvent effects can have a dramatic effect on the resonance Raman spectrum for molecules involving CT states, as was shown in a previous study of rhodamine 6G.[25]

Carbazole/TCNE. The optimized structure for the carbazole/TCNE complex is shown in Figure 4. Results for the calculation of vertical excitations and transition dipole moments using TDDFT with both XC functionals are compared with experimental findings in Table 1. For the experimental estimates for the locations of the two excitations, electronic structure calculations involving the Pariser−Parr−Pople (PPP)[62] and semiempirical AM1 methods[36] were used to determine that the HOMO and HOMO-1 of carbazole are energetically similar. These analyses were performed for the carbazole donor in vacuum and, therefore, do not include interactions with the TCNE acceptor molecule. The calculations presented in this work include the entire complex as shown in Figure 4, and when TDDFT was applied using the LC-ωPBE functional to the carbazole/TCNE complex, it was determined that two CT states exist in energetically close proximity for this complex. When the calculation is performed using B3LYP the excitation energies are severely underestimated for both CT states, which has been observed previously in the literature and can be traced to self-interaction errors resulting from missing HF exchange.[60] These states will be referred to as the CT1 and CT2 states in the discussion that follows. Having two states in the absorbance band confirms what was proposed in refs 36 and 62.

Inspection of the transition dipole moments in Table 1 indicates that each method gives a different description of both excited states. This is reflected in the very different simulation of the absorbance spectrum (see Figure 5) for each method. For B3LYP, the CT2 state is more intense than the CT1 state, and as a result, the CT2 state must be positioned near the absorbance maximum to obtain a good description. The LC-ωPBE functional finds that the two states have similar intensity and are positioned nearly equidistant from the absorbance maximum. Experimentally, the transition dipole moments were determined as fitting parameters that gave the best agreement with the resonance Raman spectra.[36]
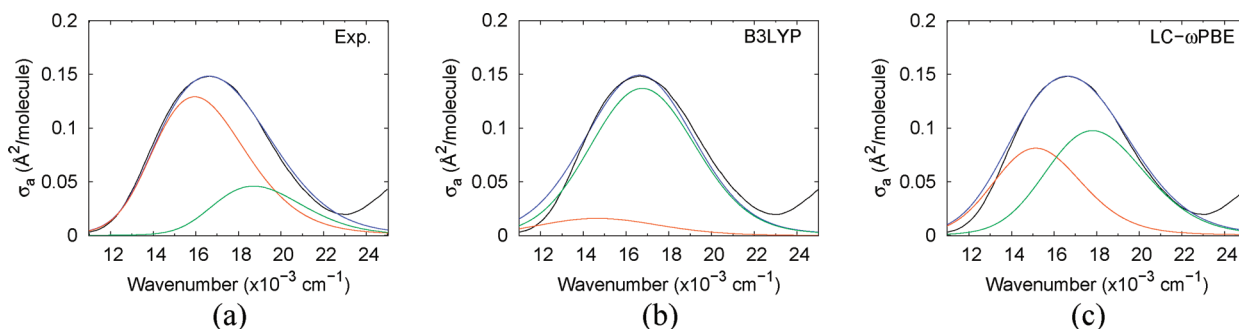

Figure 5. Absorbance spectra for carbazole/TCNE with fits compared to the experimental absorbance spectrum (black line, ref 36). In the figures, the total fit is the blue line, the fit for the CT1 state (at lower energy) is the red line, and the fit for the CT2 state (at higher energy) is the green line. The fit labeled "Exp." used $\Gamma_{CT1} = 300$ cm^{-1}, $\Gamma_{CT2} = 200$ cm^{-1}, $\Theta = 1200$ cm^{-1}, scale factor = 0.732. Using the B3LYP functional: $\Gamma_{CT1} = 250$ cm^{-1}, $\Gamma_{CT2} = 300$ cm^{-1}, $\Theta = 2200$ cm^{-1}, scale factor = 0.893. For LC-ωPBE: $\Gamma_{CT1} = 300$ cm^{-1}, $\Gamma_{CT2} = 250$ cm^{-1}, $\Theta = 1600$ cm^{-1}, scale factor = 2.01.
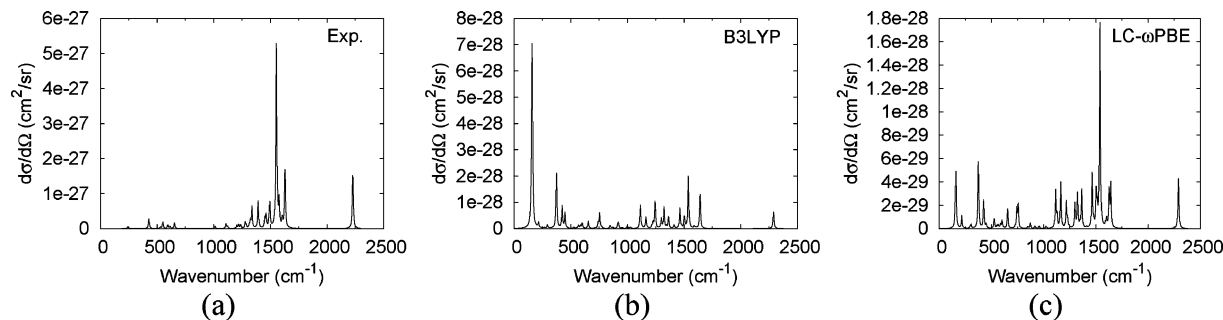
Figure 6. Resonance Raman spectra at 601 nm for carbazole/TCNE using the optimum modeling parameters for the absorbance spectra plotted in Figure 5. Data for the spectrum labeled "Exp." are from ref 36. Spectra are broadened with a Lorentzian function with 10 cm^{-1} width.
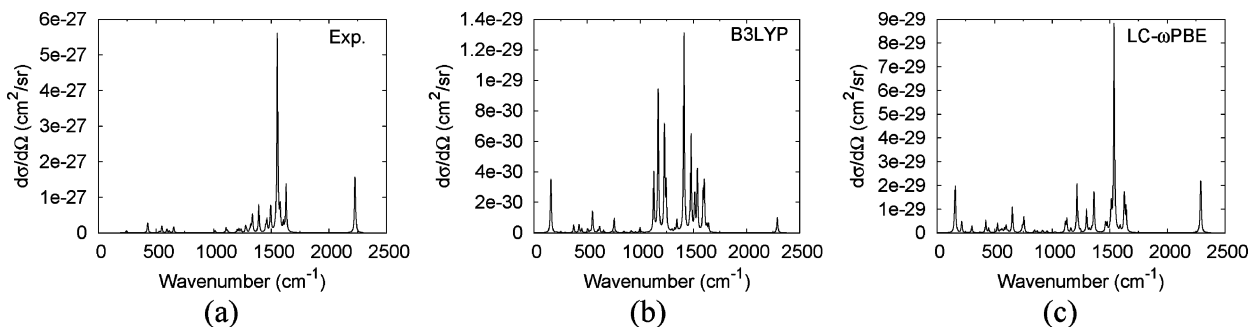

Figure 7. Individual resonance Raman spectra for the CT1 state at 601 nm for the carbazole/TCNE complex using the optimum modeling parameters for the absorbance spectra plotted in Figure 5. Data for the spectrum labeled "Exp." are from ref 36. Spectra are broadened with a Lorentzian function with 10 cm^{-1} width.

In this case, it is found that the CT1 state is more intense and is positioned closer to the absorbance maximum than the CT2 state resulting from the transition dipole moments.

In Figure 5, plots of the fits using the experimental, B3LYP, and LC-ωPBE Δ_k^n values (see Tables 6–8 in the Supporting Information) are shown. For this system, the CT1 state involves the HOMO to LUMO excitation regardless of which functional is used. The CT2 state is a transition between the HOMO-1 and LUMO for both functionals. Both functionals yield similar character for the orbitals involved in both CT states, where the HOMO and HOMO-1 are localized on the carbazole molecule, and the LUMO is contributed to by the TCNE molecule. The simulated absorbance spectrum is especially good for the LC-ωPBE functional. However, both XC functionals yield a poorer fit than experimentally determined parameters for the red-edge of the absorbance maximum.

Simulated resonance Raman spectra at the absorbance maximum (601 nm) are shown in Figure 6. At that wavelength both CT states have some contribution to the total resonance Raman spectrum. A simple qualitative examination of the spectra indicates again that B3LYP overestimates the contribution of the intermolecular D–A stretch at 159.78 cm^{-1}. Even if that mode were ignored, the mode at 1537.44 cm^{-1} would not stand out on the resonance Raman spectrum even though that mode (predominantly the C=C stretch of the TCNE molecule) is the dominant feature observed experimentally. Clearly, the potential energy surfaces of the CT1 and CT2 states are poorly described by B3LYP, as indicated by the resonance Raman spectrum.

LC-ωPBE yields a spectrum where the correct mode is the dominant feature of the spectrum but also has some noticeable differences. The fact that the relative intensities of the modes at 1537.44, 1602.16 (carbazole C–H and N–H in-plane bending and ring deformations), and 2287.67 cm^{-1} (TCNE CN stretch) are nearly identical to experiment demonstrates that this functional is giving a better description of the potential energy surfaces of the CT1 and CT2 states. Differences present on the spectrum below 1500 cm^{-1} between the LC-ωPBE functional and the experiment result in part from the energetic placement of the excited states to obtain good fits and also in particular the transition dipole moments for the two states. Because the experimental fit determines that CT2 has a significantly smaller transition dipole moment, this state will not be observed having as strong of an effect on the resonance Raman spectrum. LC-ωPBE finds that the transition dipole moments for both states have similar magnitude, causing a noticeable contribution from both states to the resonance Raman spectrum.

To determine the effects of the different excited states, resonance Raman spectra for the individual CT1 and CT2 (Figures 7 and 8) states were simulated by only including one excited state. Comparing the results for the CT1 state alone, it is clear that LC-ωPBE gives a very similar resonance Raman spectrum compared with the experimental result. It is also distinct that the description from B3LYP is poor, likely resulting from the same incorrect behavior of the XC potential for B3LYP described above for the HMB/TCNE complex. Only a few modes around 750 and 1250 cm^{-1}, involving carbazole ring deformations and in-plane bending
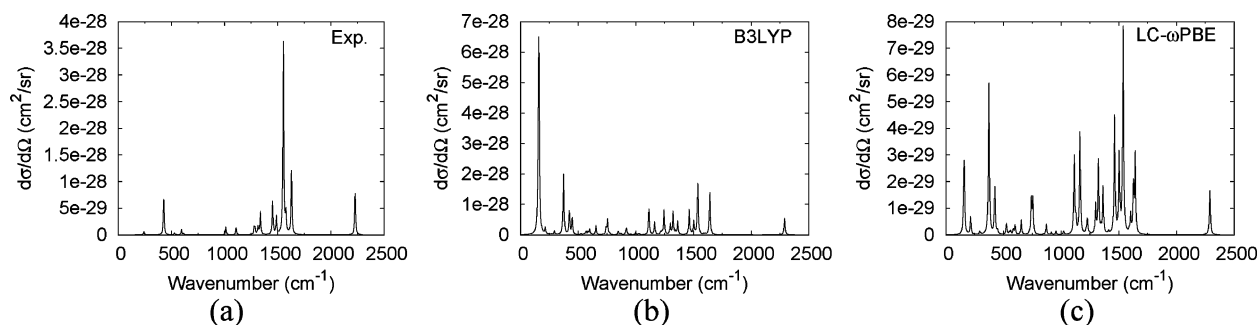
Figure 8. Individual resonance Raman spectra for the CT2 state at 601 nm for carbazole/TCNE complex using the optimum modeling parameters for the absorbance spectra plotted in Figure 5. Data for the spectrum labeled "Exp." are from ref 36. Spectra are broadened with a Lorentzian function with 10 cm^{-1} width.

of C−H and N−H bonds, have intensities that are overestimated by the LC-ωPBE functional.

A comparison between the resonance Raman spectra for the individual CT1 and CT2 states from the LC-ωPBE functional and experimental data gives an indication of how well each excited state is described using the LC-DFT method. The CT1 state simulated by LC-ωPBE compares well with what is found from experiment, indicating that this state is described correctly by the LC-ωPBE functional. When the CT2 state is simulated, there is a clear difference between what is observed experimentally and using the LC-ωPBE functional, however, due to the appearance of two modes with high intensity near 425 cm^{-1} (carbazole out of plane ring deformation) and also several high-intensity modes between 1000 and 1500 cm^{-1} for the LC-ωPBE model. This disagreement stands out, but based on the agreement of LC-ωPBE with experiment for the CT1 state, it does not seem like the description of the CT2 state potential energy surface by the LC-ωPBE is necessarily incorrect.

Use of the experimental fit proposed in ref 36 would mean that observing both CT states separately is very difficult because both overlap on the blue edge of the absorbance maximum. Although interference effects[36] are observed between the two CT states, this does not seem to be the reason why the Δ_k^n values for the CT1 and CT2 states are so similar experimentally. Because of the large amount of overlap, the positioning of the two states and the large transition dipole moment of the CT1 state compared to the CT2 state from experiment, the CT1 state is observed to dominate the contributions to the total resonance Raman spectrum (Figure 6). As a result, any wavelength used to measure a resonance Raman spectrum for the carbazole/TCNE complex would have intensities largely derived from the CT1 state. Likely, the CT2 state was only partially observed due to changes in relative peak intensities on the total resonance Raman spectrum, but its contribution was so weak that it could not be fully resolved.

Because the CT1 and CT2 states overlap to some degree in the absorbance spectrum there is a possibility that interference effects may occur in the resonance Raman spectrum. Interference can be constructive and result in an increased total differential cross-section compared to the individual contributions of either CT states or destructive which causes a reduction in peak intensities for specific modes on the total resonance Raman spectrum.[39] These

effects are described in detail in ref 36 for parallel transition dipole moments and more generally in ref 39 for numerous situations involving different modeling parameters. Three important cases that may cause destructive interference are having: Δ_k^n values with opposite signs, the angle between the transition dipole moments of different states, and detuning from resonance.

The contribution from Δ_k^n values with opposite signs is important because for two contributing excited states the differential Raman scattering cross-section is proportional to the sum of the polarizability of each state squared. This causes terms in the differential Raman scattering cross-section that are products of the polarizability of each state that both depend on the Δ_k^n values as multiplicative factors. The angle between the transition dipole moments for the two states can result in components of the transition dipole moments that are opposite in sign. For the experimental spectrum, it was assumed that the transition dipoles are parallel,[36] but LC-ωPBE finds that there is a 125.5° angle between them. This means that only the first effect is present in the total resonance Raman spectrum for the experimental data, but both are present for the LC-ωPBE functional. The third effect was elaborated on in ref 39 and is caused by detuning from resonance with the excited states resulting in resonance deenhancement. This third effect can be observed when changing the excitation wavelength along the absorbance peak and is clearly viewed for the experimental data, where the sign of the Fourier integrals can change and result in different signs for the real and imaginary components of the polarizability. This effect is most clear when the sum-over-states expression for the Raman polarizability is examined, where having an excitation wavelength greater than the vertical excitation energy creates a negative sign in the energy denominator.

The interference effects, I, in terms of the resonance Raman cross-sections for this system can be quantified as

$$I = \left(\frac{d\sigma}{d\Omega}\right)_{\text{total}} - \left(\frac{d\sigma}{d\Omega}\right)_{\text{CT1}} - \left(\frac{d\sigma}{d\Omega}\right)_{\text{CT2}} \quad (13)$$

where the terms on the right-hand side are, respectively, the total differential Raman cross-section, the differential Raman cross-section for the CT1 state alone, and the differential Raman cross-section for the CT2 state alone. This allows plots of interference to be made over the spectral range of
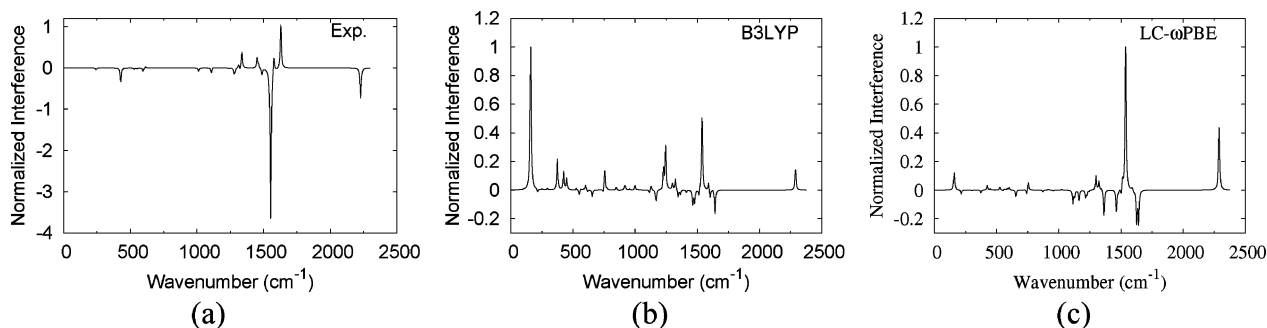
Figure 9. Plots of the interference between the CT1 and CT2 states at 601 nm using eq 13. Plots are normalized to the peak with maximum constructive interference. Data for the spectrum labeled "Exp." are from ref 36.

the resonance Raman spectrum, like what is shown in Figure 9. For each plot, data are normalized to the mode with maximum constructive interference, and thus, any negative peak represents destructive interference.

An obvious difference is apparent by investigating the interference patterns presented in Figure 9. First, the figure derived from experimental data has constructive interference present for modes involving Δ_k^n values that are opposite in sign for the CT1 and CT2 states. This disagrees with the analysis presented in ref 36, where having Δ_k^n values with opposite signs for the CT1 and CT2 states was thought to be the only factor causing destructive interference. Because the transition dipole moments are parallel (directed along the positive z-axis), their components have the same sign and cannot result in destructive interference effects. This means that the third effect resulting from the sign of the integral must lead to the seemingly opposite picture for the constructive and destructive interference observed for the experimental data. A test calculation (data not shown) where the experimental absorbance maxima for CT1 and CT2 were shifted to the locations determined for the best fit of the LC-ωPBE functional caused the interference pattern to change from what is shown in Figure 9 to a pattern similar to that found for LC-ωPBE, indicating that this detuning effect is important for determining interference. Also, it can be shown that the interference pattern changes when data is compared at different excitation wavelengths for the experimental data (see Figure 1 in the Supporting Information).

For both the B3LYP and LC-ωPBE functionals, all three interference effects are present, resulting in a different description of the interference pattern. Although the magnitude of constructive interference for the B3LYP functional, particularly on the low-frequency side of the spectrum, does not agree with the description by LC-ωPBE, examination of the interference plots show that many of the same modes have constructive interference. This is surprising based on the poor description of the potential energy surfaces by B3LYP, but more importantly it demonstrates that all three effects discussed above are important for describing interference. It turns out that out of eight modes found experimentally to have destructive interference, six of these modes at 617.00, 1127.24, 1362.96, 1463.04, 1477.85, and 1626.19 cm^{-1} were found to show destructive interference using the LC-ωPBE functional.

One final detail is the vibrational reorganization energy for the carbazole/TCNE system. Experiment finds compa-

rable values for the CT1 and CT2 states of 1988 and 1950 cm^{-1}, respectively. The respective values are 2441 and 1456 cm^{-1} for B3LYP and 1375 and 2606 cm^{-1} for LC-ωPBE. Due to the different descriptions of the two CT states using B3LYP and LC-ωPBE as compared with experiment, it is difficult to directly compare the individual reorganization energies. However, the sum of the reorganization energies for the two CT states are similar in all three cases.

Conclusions

This work presents the first application of the long-range corrected density functional theory (LC-DFT) method to resonance Raman scattering of donor–acceptor complexes. The popular global hybrid functional B3LYP and LC-functional LC-ωPBE were compared against experimental data for the carbazole/tetracyanoethylene (TCNE) and hexamethylbenzene/TCNE donor–acceptor complexes with important charge transfer (CT) states in their optical absorbance spectra. Using simulations of the absorbance and resonance Raman spectra involving the time-dependent formalism of Heller et al., it was found that, even though B3LYP could simulate absorbance spectra reasonably, it yielded poor descriptions of the excited-state potential energy surfaces in the FC region, as indicated by resonance Raman spectra. The LC-ωPBE functional simulates the absorbance spectra well and significantly improves the description of the potential energy surfaces in the FC region, as shown by its better agreement with the experimental resonance Raman spectrum for both complexes. For the carbazole/TCNE complex in particular the overlapping CT1 and CT2 states cause interference effects that change relative peak intensities on the resonance Raman spectrum. These effects can be traced to three factors: the sign of Δ_k^n for each state, the angle between the transition dipole moments, and detuning from resonance with each state. In the analysis we showed that all three factors need to be accounted for. Finally, the total vibrational reorganization energy from both B3LYP and LC-ωPBE was compared to what was calculated experimentally using the Marcus theory of electron transfer.[9] Both functionals yield reasonable predictions of the total vibrational reorganization energy, but LC-ωPBE distributes single-mode contributions similarly to what was found experimentally based on the resonance Raman spectra. In order to improve agreement with the experimental data, it might be necessary to include solvent effects in these systems so that the Δ_k^n

values compare more closely with experiment for the CT states investigated in this work.[25]

Supporting Information Available: Data tables containing the Δ_k^n values, single-mode reorganization energies, normal mode assignments from the experimental and B3LYP data, and figures showing the interference patterns at several excitation wavelengths. This information is available free of charge via the Internet at http://pubs.acs.org/.

References

(1) Wang, X.; Maeda, K.; Chen, X.; Takanabe, K.; Domen, K.; Hou, Y.; Fu, X.; Antonietti, M. *J. Am. Chem. Soc.* **2009**, *131*, 1680.

(2) Wang, X.; Maeda, K.; Thomas, A.; Takanabe, K.; Xin, G.; Carlsson, J. M.; Domen, K.; Antonietti, M. *Nat. Mater.* **2009**, *8*, 76.

(3) Brabec, C. J.; Zerzaa, G.; Cerullob, G.; Silvestrib, S. D.; Luzzatic, S.; Hummelend, J. C.; Sariciftci, S. *Chem. Phys. Lett.* **2001**, *340*, 232.

(4) Page, C. C.; Moser, C. C.; Chen, X.; Dutton, P. L. *Nature* **1999**, *402*, 47.

(5) Liu, Z.; Zhang, C.; He, W.; Qian, F.; Yang, X.; Gao, X.; Guo, Z. *New J. Chem.* **2010**, *34*, 656.

(6) Tseng, T.-C.; et al. *Nature Chem.* **2010**, *2*, 374.

(7) Hupp, J. T.; Williams, R. D. *Acc. Chem. Res.* **2001**, *34*, 808.

(8) Barbara, P. F.; Meyer, T. J.; Ratner, M. A. *J. Phys. Chem.* **1996**, *100*, 13148.

(9) Marcus, R. A. *J. Chem. Phys.* **1965**, *43*, 679.

(10) Myers, A. B. *Chem. Rev.* **1996**, *96*, 911.

(11) Biswas, N.; Umapathy, S. *Chem. Phys. Lett.* **1998**, *294*, 181.

(12) Hoekstra, R. M.; Zink, J. I.; Telo, J. P.; Nelsen, S. F. *J. Phys. Org. Chem.* **2009**, *22*, 522.

(13) Albrecht, A. C. *J. Chem. Phys.* **1961**, *34*, 1476.

(14) Albrecht, A. C.; Hutley, M. C. *J. Chem. Phys.* **1971**, *55*, 4438.

(15) Tang, J.; Albrecht, A. C. *J. Chem. Phys.* **1968**, *49*, 1144.

(16) Tannor, D. J.; Heller, E. J. *J. Chem. Phys.* **1982**, *77*, 202.

(17) Heller, E. J. *Acc. Chem. Res.* **1981**, *14*, 368.

(18) Heller, E. J.; Sundberg, R.; Tannor, D. *J. Phys. Chem.* **1982**, *86*, 1822.

(19) Lee, S.-Y.; Heller, E. J. *J. Chem. Phys.* **1979**, *71*, 4777.

(20) Petrenko, T.; Neese, F. *J. Chem. Phys.* **2007**, *127*, 164319.

(21) Neese, F.; Petrenko, T.; Ganyushin, D.; Olbrich, G. *Coord. Chem. Rev.* **2007**, *251*, 288.

(22) Kelley, A. M. *J. Phys. Chem. A* **2008**, *112*, 11975.

(23) Kane, K. A.; Jensen, L. *J. Phys. Chem. C* **2010**, *114*, 5540.

(24) Guthmuller, J.; Champagne, B. *J. Chem. Phys.* **2007**, *127*, 164507.

(25) Guthmuller, J.; Champagne, B. *J. Phys. Chem. A* **2008**, *112*, 3215.

(26) Dreuw, A.; Weisman, J. L.; Head-Gordon, M. *J. Chem. Phys.* **2003**, *119*, 2943.

(27) Bernasconi, L.; Sprik, M.; Hutter, J. *J. Chem. Phys.* **2003**, *119*, 12417.

(28) Neugebauer, J.; Louwerse, M. J.; Baerends, E. J.; Wesolowski, T. A. *J. Chem. Phys.* **2005**, *122*, 094115.

(29) Lange, A.; Herbert, J. M. *J. Chem. Theory Comput.* **2007**, *3*, 1680.

(30) Iikura, H.; Tsuneda, T.; Yanai, T.; Hirao, K. *J. Chem. Phys.* **2001**, *115*, 3540.

(31) Vydrov, O. A.; Scuseria, G. E. *J. Chem. Phys.* **2006**, *125*, 234109.

(32) Yanai, T.; Tew, D. P.; Handy, N. C. *Chem. Phys. Lett.* **2004**, *393*, 51.

(33) Livshits, E.; Baer, R. *Phys. Chem. Chem. Phys.* **2007**, *9*, 2932.

(34) Baer, R.; Neuhauser, D. *Phys. Rev. Lett.* **2005**, *94*, 043002.

(35) Stein, T.; Kronik, L.; Baer, R. *J. Am. Chem. Soc.* **2009**, *131*, 2818.

(36) Egolf, D. S.; Waterland, M. R.; Kelley, A. M. *J. Phys. Chem. B* **2000**, *104*, 10727.

(37) Markel, F.; Ferris, N. S.; Gould, I. R.; Myers, A. B. *J. Am. Chem. Soc.* **1992**, *114*, 6208.

(38) Kulinowski, K.; Gould, I. R.; Myers, A. B. *J. Phys. Chem.* **1995**, *99*, 9017.

(39) Shin, K.-S. K.; Zink, J. I. *J. Am. Chem. Soc.* **1990**, *112*, 7148.

(40) Wootton, J. L.; Zink, J. I. *J. Am. Chem. Soc.* **1997**, *119*, 1895.

(41) Kramers, H. A.; Heisenberg, W. *Z. Phys.* **1925**, *31*, 681.

(42) Dirac, P. A. M. *Proc. R. Soc. London, Ser. A* **1927**, *114*, 710.

(43) Neugebauer, J.; Reiher, M.; Kind, C.; Hess, B. A. *J. Comput. Chem.* **2002**, *23*, 895.

(44) Craig, D. P.; Thirunamachandran, T. *Molecular Quantum Electrodynamics: An Introduction to Radiation Molecule Interactions*; Dover Publications, Inc.: Mineola, NY, 1998; pp128−141.

(45) Long, D. A. *The Raman Effect: A Unified Treatment of the Theory of Raman Scattering by Molecules*; John Wiley & Sons, Ltd.: West Sussex, England, 2002; pp 85−152, 221−270.

(46) Neugebauer, J.; Hess, B. A. *J. Chem. Phys.* **2004**, *120*, 11564.

(47) Reiher, M.; Neugebauer, J.; Hess, B. A. *Z. Phys. Chem.* **2003**, *217*, 91.

(48) Straatsma, T.P.; Apra, E.; Windus, T.L.; Bylaska, E.J.; de Jong, W.; Hirata, S.; Valiev, M.; Hackler, M.; Pollack, L.; Harrison, R.; Dupuis, M.; Smith, D.M.A; Nieplocha, J.; Tipparaju V.; Krishnan, M.; Auer, A.A.; Brown, E.; Cisneros, G.; Fann, G.; Früchtl, H.; Garza, J.; Hirao, K.; Kendall, R.; Nichols, J.; Tsemekhman, K.; Wolinski, K.; Anchell, J.; Bernholdt, D.; Borowski, P.; Clark, T.; Clerc, D.; Dachsel, H.; Deegan, M.; Dyall, K.; Elwood, D.; Glendening, E.; Gutowski, M.; Hess,

Donor−Acceptor Complexes

J. Chem. Theory Comput., Vol. 6, No. 9, 2010 **2855**

A.; Jae, J.; Johnson, B.; Ju, J.; Kobayashi, R.; Kutteh, R.; Lin, Z.; Littleeld, R.; Long, X.; Meng, B.; Nakajima, T.; Niu, S.; Rosing, M.; Sandrone, G.; Stave, M.; Taylor, H.; Thomas, G.; van Lenthe, J.; Wong, A.; Zhang, Z. *NWChem, A Computational Chemistry Package for Parallel Computers*, version 5.1, a modified version; Pacific Northwest National Laboratory: Richland, WA, 2007.

(49) Jensen, L.; Govind, N. *J. Phys. Chem. A* **2009**, *113*, 9761.

(50) Govind, N.; Valiev, M.; Jensen, L.; Kowalski, K. *J. Phys. Chem. A* **2009**, *113*, 6041.

(51) Henderson, T. M.; Janesko, B. G.; Scuseria, G. E. *J. Chem. Phys.* **2008**, *128*, 194105.

(52) Weintraub, E.; Henderson, T. M.; Scuseria, G. E. *J. Chem. Theory Comput.* **2009**, *5*, 754.

(53) Rohrdanz, M. A.; Martins, K. M.; Herbert, J. M. *J. Chem. Phys.* **2009**, *130*, 054112.

(54) Becke, A. D. *J. Chem. Phys.* **1993**, *98*, 5648.

(55) Bauernschmitt, R.; Ahlrichs, R. *Chem. Phys. Lett.* **1996**, *256*, 454.

(56) Bauernschmitt, R.; Häser, M.; Treutler, O.; Ahlrichs, R. *Chem. Phys. Lett.* **1996**, *264*, 573.

(57) Rohrdanz, M. A.; Herbert, J. M. *J. Chem. Phys.* **2008**, *129*, 034107.

(58) Grimme, S. *J. Comput. Chem.* **2004**, *25*, 1463.

(59) Grimme, S. *J. Comput. Chem.* **2006**, *27*, 1787.

(60) Dreuw, A.; Head-Gordon, M. *J. Am. Chem. Soc.* **2003**, *126*, 4007.

(61) Myers, A. B.; Pranata, K. S. *J. Phys. Chem.* **1989**, *93*, 5079.

(62) Landman, U.; Ledwith, A.; Marsh, D. G.; Williams, D. J. *Macromolecules* **1976**, *9*, 833.

CT1002779